

© 2021 Sheng Yang

IRRADIATION STUDIES OF FUSED SILICA MATERIALS FOR THE ATLAS HIGH
LUMINOSITY ZERO DEGREE CALORIMETER AND DEVELOPMENT OF MACHINE
LEARNING TECHNIQUES FOR THE REACTION PLANE RECONSTRUCTION IN HEAVY
ION COLLISIONS AT THE LARGE HADRON COLLIDER

BY

SHENG YANG

PRELIMINARY EXAMINATION

Submitted in partial fulfillment of the requirements
for the degree of Doctor of Philosophy in Nuclear Plasma and Radiological Engineering
in the Graduate College of the
University of Illinois at Urbana-Champaign, 2021

Urbana, Illinois

Committee:

Matthias Perdekamp, Adviser
Rizwan Uddin
Angela Di Fulvio
Kathryn Huff
Riccardo Longo

ABSTRACT

The ATLAS Zero Degree Calorimeter (ZDC) is a sampling calorimeter that measures neutral particles on-axis to the beam at the ATLAS experiment in the Large Hadron Collider (LHC). Fused quartz was used as a Cherenkov radiator inside the ZDC design in Run 1. A significant Cherenkov light yield degradation of the fused quartz due to the radiation damage was observed after Run 1. The fused-quartz ZDC is not suitable for long-term stable operation in the High-Luminosity upgrade of the LHC (HL-LHC), since the ZDC will be exposed to higher integrated dose. Fused silica was proposed as a possible solution because of a study carried by the Beam RAtE of Neutrals (BRAN) group at LHC. Fused silica rods characterized by different OH and H₂ doping levels were installed and irradiated to study the degradation of the Cherenkov light yield. During LHC Run 2 it was found that, after an initial degradation phase, the performance of the fused silica becomes stable over a large range of irradiation. Therefore, it is possible to use the fused-silica to equip a radiation-hard ZDC that can be operated in the HL-LHC environment. This paper presents preliminary results of the optical transmission and ²²Na activity measurements of the fused silica rods irradiated in the LHC Run 2 by the BRAN group. The accumulated dosage and activity in the rods are calculated using dedicated FLUKA simulations provided by the CERN Beam-Machine Interface group (EN-STI-BMI). With the measurements and the FLUKA simulations, it was possible to study the correlation between the accumulated dosage and the transmission loss, as well as the accuracy of the activity calculated by FLUKA. The final transmission results will define the expectations for the ZDC performance stability during HL-LHC running time. The activity results represent a benchmark for the accuracy of nuclear breakup model on a wide energy range (up to the TeV scale) in FLUKA.

A novel reaction plane detector (RPD) made of fused silica fibers will be installed in the

ATLAS ZDC to measure the reaction plane (RP) in heavy-ion collisions on an event-by-event basis. Dedicated Monte Carlo simulations were carried out to estimate the signals of the RPD during mid-central heavy-ion collisions. A machine learning algorithm was used to reconstruct the event-by-event RP using the simulated RPD signals. This paper describes the simulations and the ML model and presents the performance of the algorithm and the reconstructed RP resolution in mid-central heavy-ion collision. The dependence on physics modeling is also discussed.

TABLE OF CONTENTS

LIST OF TABLES	v
LIST OF FIGURES	vi
CHAPTER 1 INTRODUCTION	1
1.1 The Large Hadron Collider (LHC)	1
1.2 ATLAS Zero Degree Calorimeter (ZDC) and Reaction Plane Detector (RPD)	1
1.3 High-Luminosity LHC	4
1.4 Beam RAt of Neutrals (BRAN) prototype	6
CHAPTER 2 IRRADIATED FUSED SILICA STUDIES: ACTIVATION AND TRANSMISSION	8
2.1 FLUKA simulation	8
2.2 Activation study for the BRAN samples	11
2.3 Transmission measurements for the BRAN samples	18
CHAPTER 3 REACTION PLANE RECONSTRUCTION FOR RPD	24
3.1 Simulation setup	24
3.2 Reaction plane reconstruction	27
CHAPTER 4 CONCLUSIONS AND FUTURE WORK	32
CHAPTER 5 REFERENCES	34

LIST OF TABLES

1.1	The integrated luminosity and maximum integrated dose estimates in the TAN/TAXN in Run 2, 3 and 4, based of FLUKA simulations provided by the EN-STI-BMI team	5
1.2	Specifications of fused silica rods in the BRAN prototype.	7
2.1	Specifications for ^{22}Na volume source	12
2.2	Specifications for HPGe Detector	13
2.3	Specifications of the well-type detector at ANL	13

LIST OF FIGURES

1.1	The plan view of ATLAS interaction point and the TAN in Run 1-3	2
1.2	Visualization of a heavy-ion collision geometry. ψ_{RP} is defined by the plane formed by the impact parameter and the beam axis. ϕ is defined by the transverse position of the spectator and the beam axis.	3
1.3	Comparison between brand new GE214 fused quartz rods (right) and the same type of rods irradiated in the LHC during Run 1 (~ 10 MGy, left).	5
1.4	TAN setup during $p+p$ running in LHC Run 2 (2016-2018). The dashed lines identify the slot used to install the ZDC during the heavy ion runs. The right insert shows a detailed top view of the BRAN prototype. The numbers identify the position of the fused silica rods. Detailed information on the materials of the rods and maximum irradiation reached for each of them are reported in Tab. 1.2	7
2.1	Dosage X-Z profile in the TAN accumulated during 2016 (upper) and 2017 (lower) proton-proton collision ($p+p$) runs, respectively. The module in the bold black box indicates the BRAN and BRAN prototype. The black lines indicate the copper block. The delivered luminosity was 45 and 50 fb^{-1} in 2016 and 2017, respectively. Please note that the color scale for 2016 and 2017 is different.	10
2.2	Dosage Y-Z profile in the BRAN prototype in 2016 (right) and 2017 (left) respectively. The crossing angle in each year has been included in the simulation, as is evident from the vertical shift in the maximum exposure position. The delivered luminosity in 2016 and 2017 was 45 and 50 fb^{-1} , respectively.	11
2.3	Comparison of Rod 1 activity measurements performed at UIUC, using a HPGe detector (Sec. 2.2.3), and ANL, using a well-type detector (Sec. 2.2.4). The dotted line is the fit of the ratio between the two measurements. The green line represents the error on calibration source activity. This uncertainty is not independent between the two measurements. Results have been normalized to a reference date of 12/14/2019.	17

2.4	Comparison of Rod 3b activity measurements performed at UIUC, using a HPGe detector (Sec. 2.2.3), and ANL, using a well-type detector (Sec. 2.2.4). The dotted line is the fit of the ratio between the two measurements. The green line represents the error on calibration source activity. This uncertainty is not independent between the two measurements. Results have been normalized to a reference date of 12/14/2019.	17
2.5	Comparison of activity Rod 6 measurements performed at UIUC, using a HPGe detector (Sec. 2.2.3), and ANL, using a well-type detector (Sec. 2.2.4). The dotted line is the fit of the ratio between the two measurements. The green line represents the error on calibration source activity. This uncertainty is not independent between the two measurements. Results have been normalized to a reference date of 12/14/2019.	18
2.6	Comparison of activity measurements at ANL, using a well-type detector, and FLUKA simulations for Rod 1. Results have been normalized to a reference date of 12/14/2019. The dotted line is the fit of ratio between data and simulations.	19
2.7	Comparison of activity measurements at ANL, using a well-type detector, and FLUKA simulations Rod 3b. Results have been normalized to a reference date of 12/14/2019. The dotted line is the fit of ratio between data and simulations.	19
2.8	Comparison of activity measurements at ANL, using a well-type detector, and FLUKA simulations Rod 6. Results have been normalized to a reference date of 12/14/2019. The dotted line is the fit of ratio between data and simulations.	20
2.9	The experimental setup for the transmission measurement. The right insert shows interior of the holder. The solid cylindrical volume indicates the position of the sample inside the holder. The light is incident on the curved side of the sample.	20
2.10	The spectral intensity of the reference sample, the baseline, and a Rod 3b sample. The center of the Rod 3b sample corresponds to 4.5 cm from the highly irradiated end of the uncut rod.	21
2.11	The spectral transmittance of the 2.5 cm of Rod 3b. There are 2 color centers (valleys) at 240 and 320 nm.	22
2.12	The transmittance at 240 nm color center for Rod 1, 3b, 5 and 6. The position starts from the highly irradiated end. The transmittance decays as the integrated dosage increases.	23
3.1	The ZDC module consists the electromagnetic (EM), RPD, and the hadronic (HAD) sections.	25
3.2	The fiber channel pattern of the RPD routed to the PMT above. The right insert shows the arrangement of the fibers in the detector. Different fiber colors identify fibers of different length.	26
3.3	Visualization of the deep learning model for reaction plane reconstruction.	28

3.4	Visualization of the Q-vector for the computing methods. The blue dots indicate the injected neutron position in the simulation.	29
3.5	Residuals distribution between the the particle level RP angle and the RP angle measured by arm A of the ZDC (left) and the true RP angle and measured RP(right).	30
3.6	Reaction plane resolution estimated using the two sub-reaction planes measured by the two arms of the ZDC. The results are presented for four different simulations where the transverse momentum kick along the direction of the reaction plane, p_T^{spec} , was varied. The vertical dashed lines correspond to the limits of the four bins in neutron multiplicity where the resolution was evaluated. Error bars are contained within the markers.	31

CHAPTER 1

INTRODUCTION

1.1 The Large Hadron Collider (LHC)

The Large Hadron Collider (LHC) [1] is the highest-energy particle accelerator in the world. A collider is a type of particle accelerator with two directed beams of particles. In the LHC, the particles are bunched together, accelerated to very high kinetic energies, and collided with other bunches at an interaction point (IP). There are multiple IPs with detectors to measure the byproducts of these collisions for different physics purposes. For example, ATLAS (IP1) and CMS (IP5) are general-purpose particle detector experiments, while ALICE (IP2) is a dedicated experiment for heavy-ion collisions, and LHCb (IP8) is a specialized bottom quark experiment. [2, 3, 4, 5, 6]. This work focuses on the material used in the Zero Degree Calorimeter (ZDC) of the ATLAS experiment.

1.2 ATLAS Zero Degree Calorimeter (ZDC) and Reaction Plane Detector (RPD)

1.2.1 Zero Degree Calorimeter

The ATLAS ZDC [7, 3] is used to measure neutral particles on-axis to the beam. In heavy-ion collisions, neutrons not directly involved in the collision, known as “spectator” neutrons, will continue to travel along the collision axis while charged particles and fragments are deflected due to the beam optics [8]. ZDCs are integrated with the Target Absorber for Neutrals (TAN), located at ± 140 from the IP in LHC. Fig. 1.1 shows the plan view of the sections between the IP and the ZDCs in Run 1-3. Note that the upgraded TAN (TAXN)

and ZDCs will be located to ± 127 from the IP in Run 4.

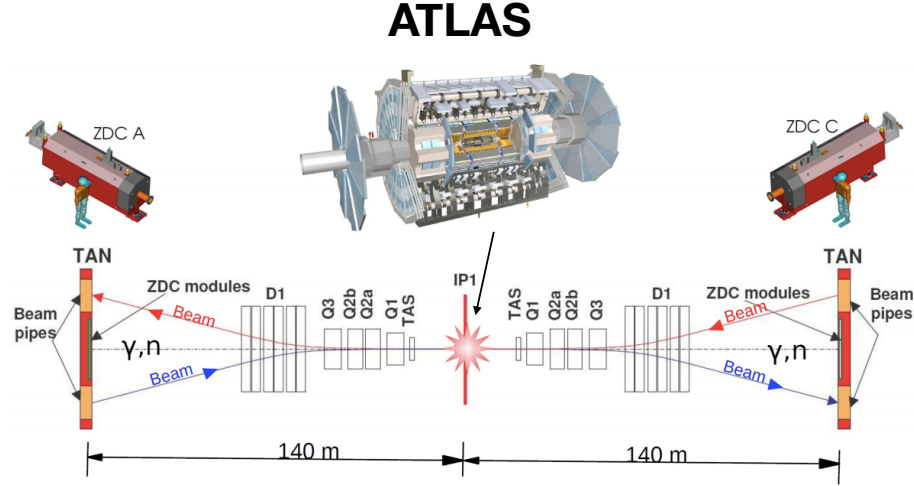


Figure 1.1: The plan view of ATLAS interaction point and the TAN in Run 1-3 [8].

The ZDC is a sampling calorimeter that detects neutrons using Cherenkov light. When the spectator neutrons interact with the ZDCs, a shower of particles is created from hadronization. When the charged component of the particles passes through the active element made of quartz rods in the ZDC, the Cherenkov light is generated and transported to the top of the rods by total internal reflection. The light is collected by a light guide above the ZDC and converted to electronic signals by photomultiplier tubes (PMTs).

1.2.2 Reaction plane detector

During heavy-ion collisions, an anisotropic azimuthal distribution of particles, known as flow, is observed due to high pressure arising from compression and heating of nuclear matter [9]. The n^{th} flow component, v_n , can be obtained in the Fourier-series with respect to the reaction plane, spanned by the vector of the impact parameter and the beam direction [10]:

$$E \frac{d^3N}{d^3p} = \frac{1}{2\pi} \frac{d^2N}{p_T dp_T dy} \left(1 + 2 \sum_{n=1}^{\infty} v_n \cos[n(\phi - \psi_{RP})] \right), \quad (1.1)$$

where ψ_{RP} is the reaction plane angle and p_T is the transverse momentum. Fig. 1.2 shows a visualization of a heavy-ion collision geometry.

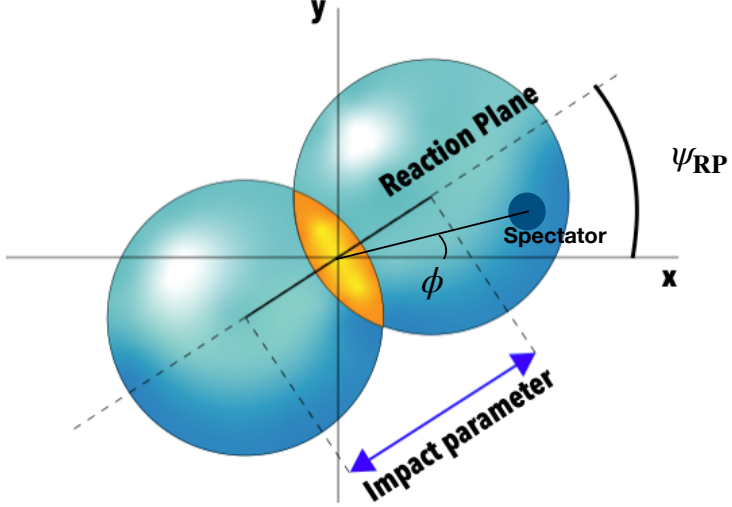


Figure 1.2: Visualization of a heavy-ion collision geometry. ψ_{RP} is defined by the plane formed by the impact parameter and the beam axis. ϕ is defined by the transverse position of the spectator and the beam axis.

The coefficient v_1 , better known as directed flow, provides a measurement of the asymmetry in the particle production along the reaction plane direction. In other words, a non-zero directed flow indicates the presence of a preferential direction for the particle emission during the collision. A key ingredient to determine v_1 is the measurement of the reaction plane making use of the spectators of the collision.

A reaction plane detector (RPD) in the ZDCs of ATLAS has been proposed to estimate the reaction plane angle of individual heavy-ion collisions during Run 3 and 4. The proposed RPD is a 2-dimensional array of fused silica fibers with varying lengths. The RPD can capture the transverse profile of the showers generated in the upstream section. With the captured profile, it is possible to estimate the correlated deflection of the spectator neutrons. Then, the reaction plane can be determined from the direction of the deflection.

1.3 High-Luminosity LHC

Instantaneous luminosity, L , [11] is an important parameter to evaluate the number of collisions that can be produced for a particle accelerator and is defined as:

$$L = \frac{1}{\sigma_p} \frac{dR}{dt}, \quad (1.2)$$

where dR/dt is the collision rate, and σ_p is the cross section of the corresponding reaction. Instantaneous luminosity depends on the particle beam parameters, i.e., the number of particles in a bunch and the overlapping area of two bunches during the collision. Integrated luminosity, L_{int} , is an integral of the instantaneous luminosity with respect to time. The higher integrated luminosity means more data can be collected for analysis. Therefore, scientists at LHC aim to maximize the integrated luminosity.

The High-Luminosity LHC (HL-LHC) is a major upgrade of the LHC to increase the integrated luminosity [12]. The expected integrated luminosity of the HL-LHC (Run 3-4) is at least three times higher than the integrated luminosity of the current LHC (Run 2) [13]. Table 1.1 shows the current and projected integrated luminosity and integrated radiation doses in the TAN and TAXN from HL-LHC operations.

The high integrated luminosity also creates many challenges. The radiation-hardness of detectors is one of the major challenges associated with the HL-LHC upgrade. In [14], the author studied the light yield degradation of fused quartz rods used as a Cherenkov radiator in the ZDC during 2010-2012 (Run 1). There was a significant light loss across the ultraviolet and visible light range, 300 - 1000 nm, in the fused quartz rods due to the irradiation. A batch of the rods irradiated during 2011 is shown in Fig. 1.3, compared to un-irradiated samples made of the same fused quartz (GE214). The radiation exposure experienced during Run 1 was sufficient to turn the quartz almost completely opaque. The integrated luminosity in Run 1 is 22.7 fb^{-1} [15], which is only about 7% of the integrated luminosity in Run 3. Therefore, the fused-quartz-base ZDC design will not suitable for long-term operation in the HL-LHC era.

In 2017, a joint upgrade project between the ATLAS and CMS ZDC groups was started



Figure 1.3: Comparison between brand new GE214 fused quartz rods (right) and the same type of rods irradiated in the LHC during Run 1 (~ 10 MGy, left).

Run		pp	Low-μ pp	p+Pb	Pb+Pb
Run 2	CoM energy	13 TeV	5.02 TeV	8.16 TeV	5.02 TeV
	L_{int}	156 fb^{-1}	334 pb^{-1}	0.18 pb^{-1}	2 nb^{-1}
	Dose	250 MGy	210 kGy	170 kGy †	80 kGy
Run 3	CoM energy	14 TeV	5.5 - 8.8 TeV	8.8 TeV	5.5 TeV
	L_{int}	270 fb^{-1}	1.6 fb^{-1}	0.6 pb^{-1}	10 nb^{-1}
	Dose	450 MGy †	1.15 MGy †	600 kGy	450 kGy †
Run 4	CoM energy	14 TeV	5.5 - 8.8 TeV	8.8 TeV	5.5 TeV
	L_{int}	700 fb^{-1}	1.6 fb^{-1}	0.6 pb^{-1}	10 nb^{-1}
	Dose	1.15 GGy †	1.15 MGy †	600 kGy	450 kGy †

Table 1.1: The integrated luminosity and maximum integrated dose estimates in the TAN/TAXN in Run 2, 3 and 4, based of FLUKA simulations provided by the EN-STI-BMI team. The tag † indicates values projected out re-scaling by luminosity and center of mass (CoM) beam energy.

to address the radiation levels that would be experienced by each group’s ZDCs in the HL-LHC. The main goal of the project was to study the potential of synthetic fused silica as a radiation-hard Cherenkov radiator for the ZDCs. A sample of fused silica rods irradiated in Run 2 was provided by the Beam RAtE of Neutrals (BRAN) luminosity detector group. The rods are used to study the correlation between the accumulated dosage and degradation of the optical transmittance in the rods. The accumulated dosage in the rods is calculated in dedicated FLUKA simulations provided by the Sources, Targets, and Interactions CERN group (EN-STI-BMI).

1.4 Beam RAtE of Neutrals (BRAN) prototype

A BRAN prototype [16] was installed to study the Cherenkov light yield degradation of different types of fused silica rods [17] characterized by the doping level of OH and H₂, and different irradiation periods. The details of the fused silica and irradiation period are given in Table 1.2. In [18], the author showed the light yield degradation results in terms of the loss of the prototype’s signal gain. After an initial significant gain loss during the first 5 fb^{-1} irradiation period, the gain of the prototype with rod 1 was found to be stable for the rest of the experimental period. It, therefore, is possible to operate a fused-silica detector in the stable gain. Although the signal loss of the prototype has been investigated, the optical transmittance degradation of irradiated fused silica rods requires further detailed studies.

BRAN Position	Irradiation Period	Max. Exposure [MGy]	Material	H_2 [mol/cm ³]	OH [ppm]
1	04/2016 - 12/2018	30	Spectrosil 2000 (High OH, Mid H_2)	7.20e17	1120
2	04/2016 - 12/2017	15	Spectrosil 2000 (High OH, Mid H_2)	7.20e17	1120
3a	04/2016 - 12/2016	5	Spectrosil 2000 (High OH, High H_2)	2.80e18	1000
3b	04/2017 - 12/2018	20	Spectrosil 2000 (High OH, Mid H_2)	7.20e17	1120
4	04/2016 - 12/2017	10	Spectrosil 2000 (High OH, H_2 free)	0	1011
5	04/2016 - 12/2017	10	Suprasil 3301 (Low OH, High H_2)	3.00e18	15
6	04/2016 - 12/2018	20	Suprasil 3301 (Low OH, H_2 free)	0	14

Table 1.2: Specifications of fused silica rods in the BRAN prototype. The number assigned to each rod corresponds to a given position in the detector, as shown in Fig. 1.4. Rods 3a and 3b occupied the same slot, but at different times.

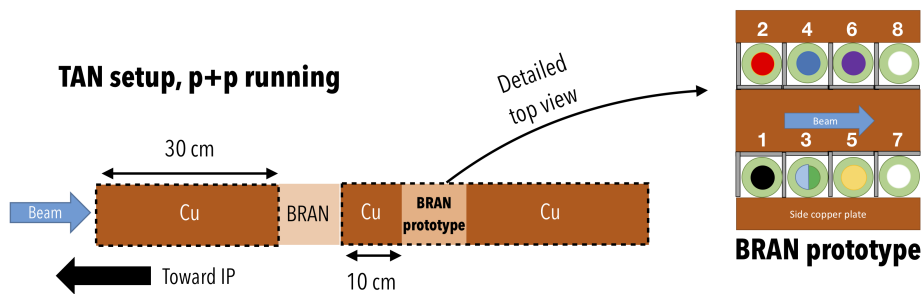


Figure 1.4: TAN setup during $p+p$ running in LHC Run 2 (2016-2018). The dashed lines identify the slot used to install the ZDC during the heavy ion runs. The right insert shows a detailed top view of the BRAN prototype. The numbers identify the position of the fused silica rods. Detailed information on the materials of the rods and maximum irradiation reached for each of them are reported in Tab. 1.2

CHAPTER 2

IRRADIATED FUSED SILICA STUDIES: ACTIVATION AND TRANSMISSION

After completion of the LHC Run 2, a sample of BRAN rods from the BRAN prototype was shipped to the University of Illinois at Urbana-Champaign for their optical transmittance and activation measurements. With support from the EN-STI-BMI team at CERN, it was possible to simulate the dosage accumulated in the BRAN rods and their activation profile, allowing for various studies to be carried out. Two such studies are the performance of FLUKA in describing ^{22}Na activation profile of the BRAN rods, discussed in Sec. 2.2, and the correlation between the accumulated dosage and the measured optical transmittance, presented in Sec. 2.3.

2.1 FLUKA simulation

The FLUKA [19] code is a general-purpose Monte Carlo code for particle interaction and transport ranging in energy from a few keV to TeV. It has been used in a broad variety of high-energy accelerator applications, including energy deposition studies associated with LHC detectors, material degradation, and residual nuclei estimation. There are extensive benchmarking studies showing an excellent agreement between simulated and measured values in the complex radiation environment of the LHC [20, 21, 22, 23].

To accurately estimate the radiation levels in the LHC, it requires a highly detailed description of the complex accelerator geometry and the associated beam optics in simulations. One key characteristic of beam optics is the crossing angle near an IP [1]. When the two LHC beams approach each other near an IP, the beams collide at an angle of a couple of hundred microradians to prevent encounters in the region where the two beams share the same vacuum chamber. A small crossing angle increases the overlap area of the bunches,

resulting in a higher collision rate. However, the angle must be large enough to mitigate the long-range interactions between the electromagnetic fields generated by the beams. The electromagnetic interactions are decreased due to the loss of intensity experienced by the beams in the collisions. By exploiting the effect, LHC scientists were able to decrease the crossing angle at IP1 from 160 μrad to 130 μrad during 2016 - 2017 runs [24].

In order to account for the different crossing angle in 2016 and 2017, two dedicated FLUKA simulations of the TAN region were produced with the following settings:

1. pp - 2016 beam configuration (160 μrad crossing angle) and delivered luminosity (45 fb^{-1}).
2. pp - 2017 beam configuration (130 μrad crossing angle) and delivered luminosity (50 fb^{-1}).

Each simulation was characterized by different beam crossing angles and irradiation times, depending on the year of LHC data taking. During 2016 and 2017 LHC runs, the rods were irradiated for 198 and 173 days, respectively.

The coordinates of the simulations follow the coordinates defined at ATLAS, where X points towards the center of the LHC tunnel, and Z is along the tunnel, and Y is in the vertical direction. Fig. 2.1 shows the X-Z profile of the dosage deposited in the TAN during the proton-proton collision ($p+p$) running in both 2016 and 2017. The corresponding projections in the Y-Z plane are shown in Fig. 2.2, where one can observe the impact of different crossing angles on the topology of the radiation deposited in the fused silica rods. Implementing this feature in the FLUKA simulation was a crucial component in accurately reproducing the activation profile along the rods. Note that it is possible to project the 2017 simulation to estimate the 2018 simulations since the 2017 and 2018 runs are characterized by the same beam configuration [25]. This step was accomplished by re-scaling the results of the 2017 simulation with the ratio of the integrated luminosity delivered by the LHC to IP1 in the two years.

Activation calculations in FLUKA require further nuclear breakup models, such as evaporation and a Fermi breakup model for light nuclei [19]. These equilibrium processes are essential for a correct calculation of residual nuclei distributions. An accurate nuclear breakup

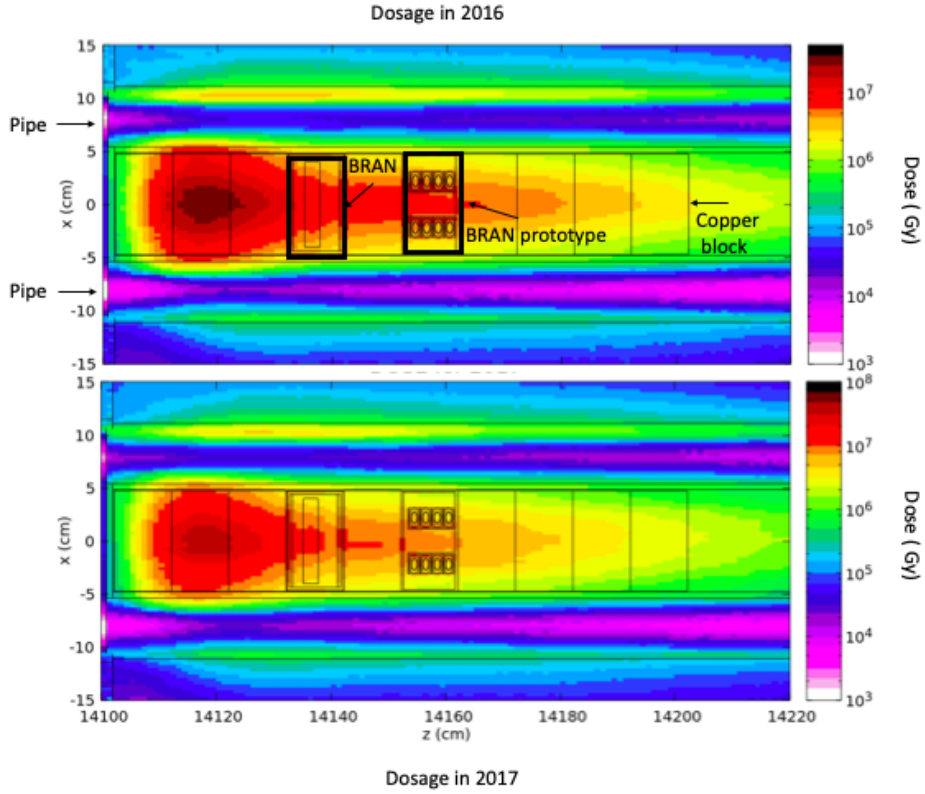


Figure 2.1: Dosage X-Z profile in the TAN accumulated during 2016 (upper) and 2017 (lower) proton-proton collision ($p+p$) runs, respectively. The module in the bold black box indicates the BRAN and BRAN prototype. The black lines indicate the copper block. The delivered luminosity was 45 and 50 fb^{-1} in 2016 and 2017, respectively. Please note that the color scale for 2016 and 2017 is different.

model is also crucial for other applications, i.e., modeling calorimeter response, since the energy spent in breaking nuclear bonds can not be compensated in the ionizing interaction. Therefore, it is essential to validate the nuclear breakup description in a simulation for reliable results. A correctly reproduced residual nuclei distribution can be proof of the accuracy of the processes in FLUKA.

The accuracy of the descriptions varies depending on the energy range of the processes. In [26], the samples were irradiated by a stray radiation field created by a 120 GeV hadron beam in a copper target. The estimated activity of the residual nuclei in the FLUKA simulations is within 30% of the measured activity. However, in [27], the samples were irradiated by a proton beam with a beam momentum of 24 GeV/c. The discrepancy between the FLUKA predicted activity and measured activity is within a factor of 2. While the

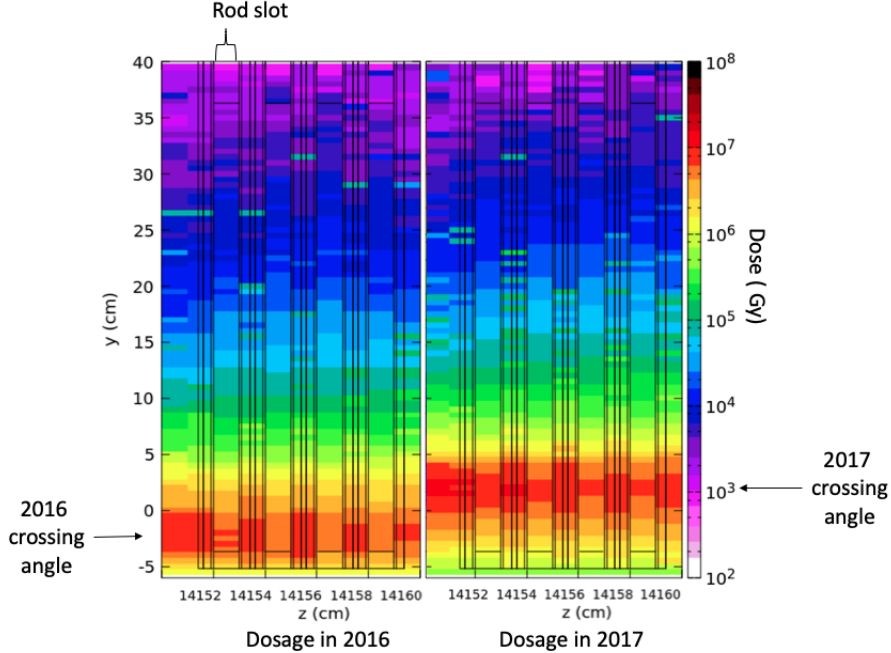


Figure 2.2: Dosage Y-Z profile in the BRAN prototype in 2016 (right) and 2017 (left) respectively. The crossing angle in each year has been included in the simulation, as is evident from the vertical shift in the maximum exposure position. The delivered luminosity in 2016 and 2017 was 45 and 50 fb^{-1} , respectively.

study supports the accuracy of the descriptions in the GeV energy range, the accuracy in the radiation field up to the TeV energy has not been validated yet. This work provides a benchmark for the accuracy of the nuclear breakup descriptions in FLUKA by measuring the activity of the residual nuclei, i.e. ^{22}Na , in BRAN rod samples.

2.2 Activation study for the BRAN samples

Two independent activation measurements were carried out at the University of Illinois Urbana-Champaign (UIUC) and Argonne National Laboratory (ANL), using a high purity germanium, HPGe, radiation detector, and a thallium activated, sodium iodide, NaI(Tl), well-type detector, respectively. In both cases, the activity of the ^{22}Na isotope in each rod segment was measured.

2.2.1 Sample preparations

The BRAN rods were cut into smaller samples to isolate the activity contribution from the rest of the rods. In addition, the transmission study necessitated having shorter rod segments to profile the BRAN rods' transmittance per unit length accurately. A length of 10 mm was chosen to meet both requirements. To account for the material loss during cutting, the weights of both the cut sample and the remaining uncut rod were recorded for each iteration. Digital calipers were used to measure the i^{th} segment's maximum length (L_i^{max}) and minimum length (L_i^{min}) by rotating the segment 360° within the calipers. The remaining rod length, L_i^{rem} , was also recorded for later calculations. The average cut length for the i^{th} segment, L_i , was then determined:

$$L_i = \left(\frac{L_i^{max} + L_i^{min}}{2} \right). \quad (2.1)$$

2.2.2 Calibrated volumetric source

To calibrate both the detectors, a customized ^{22}Na volumetric source was purchased from Eckert & Ziegler. The relevant specifications are listed in Tab. 2.1. The dimensions of the cylindrical source were chosen in order to match those of rod samples produced by cutting the irradiated BRAN rods, as described in Sec. 2.2.1. The ^{22}Na isotope is uniformly distributed throughout the source volume.

Table 2.1: Specifications for ^{22}Na volume source

Diameter	10 mm
Length	10 mm
Material	Solid plastic matrix
Density	1.17 g/cm ³ ± 3%
Isotope	^{22}Na
Activity	0.1 μ Ci ± 3.3%

2.2.3 Activation measurement using HPGe detector at UIUC

The relative efficiency and energy resolution (FWHM) of the HPGe detector used in this experiment are 19% and 1.68 keV for the 1.332 MeV peak of Co-60. A full list of specifications for the HPGe detector is given in Tab. 2.2. Each sample was measured for 15 minutes to achieve a 2% statistical error for the 1.275 MeV characteristic peak of ^{22}Na . For the ^{22}Na calibration source, the measurement time was 14 hours, corresponding to a statistical error of 0.1%. The background was measured for 24 hours and then subtracted from all the measurement results of HPGe in this study.

Table 2.2: Specifications for HPGe Detector

Model number	Ortec GEM-10-P4
Energy resolution	1.68 keV @ 1.33 MeV, Co-60
Detector diameter	4.99 mm
Detector length	54.6 mm
Relative efficiency	19% @ 1.33 MeV, Co-60

2.2.4 Activation measurement using well-type detector at ANL

A well-type detector [28], manufactured by the Perkin Elmer Company and with energy resolution <10 % for Cs-137, was used to measure the ^{22}Na activity at ANL. Its specifications are reported in Tab. 2.3. The activity of each sample was obtained from the built-in analysis software, including the uncertainty on the gamma count rate. Each sample was measured for a time sufficient to reach a statistical error less than 1% for the 1.275 MeV characteristic peak of ^{22}Na . The volumetric ^{22}Na calibration source was measured for 1 hour, achieving 0.39% statistical error.

Table 2.3: Specifications of the well-type detector at ANL

Model number	2480 Wizard gamma counters
Material	Na(Tl) crystal
Energy resolution	< 10 % for Cs-137
Crystal diameter	75 mm
Crystal height	80 mm
Relative efficiency	47% for Cs-137

2.2.5 Data analysis

In this section, the details of the gamma count rate analysis for the UIUC measurements are presented in 2.2.5.1. The activity analysis techniques, material loss, and cooling corrections applied to the measurements at UIUC and ANL are described in Sec. 2.2.5.2, 2.2.5.3, and 2.2.5.4, respectively.

2.2.5.1 Estimation of count rate for HPGe detector

The gamma count rate was estimated from the spectrum measured with the HPGe detector. The 1.275 MeV gamma peak of ^{22}Na was targeted because its branching ratio is 99.9% of ^{22}Na decay. After subtracting the background and the baseline from the targeted peak, a Gaussian fit was applied to estimate the count rate, defined as the area within the full width tenth maximum (FWTM) of the Gaussian fit.

2.2.5.2 Estimation of ^{22}Na activity

The acceptance of the experimental setup must be taken into account when estimating the activity of a volumetric isotope sample. Two types of acceptance effects are relevant for the measurement presented in this paper. The first is introduced by differences between the geometry of the calibration source and the samples. To account for this effect, the volumetric source described in Sec. 2.2.2 was used to calibrate the setup. Because the geometry of the calibrated source and the BRAN samples are consistent with one another, as well as the positioning of samples within the experimental setup, the acceptance was taken to be equivalent. This conclusion relies on the assumption that the activity of both the samples and the calibrated source is homogeneous. The second effect, introduced by the intrinsic acceptance of the experimental setup for a single photon measurement, can be canceled out by taking the ratio of the count rates recorded for the sample and calibration source.

The activity of the i^{th} sample is calculated as

$$A_i = \frac{I_i}{I_{CS}} \cdot A_{CS}, \quad (2.2)$$

where I_i and I_{CS} are the measured count rate of the i^{th} sample and the volumetric calibration source, respectively, while A_{CS} is the known activity of the calibration source. The relative uncertainty on A_i , R_{A_i} , was obtained from the error propagation of each component in Eq. 2.2 and is given as

$$R_{A_i} = \sqrt{R_{I_i}^2 + R_{I_{CS}}^2 + R_{A_{CS}}^2}, \quad (2.3)$$

where $R_X, X \in \{I_i, I_{CS}, A_{CS}\}$ represents the relative error of the variables entering Eq. 2.2.

2.2.5.3 Material loss correction

A correction was applied for the decrease in intensity of each sample due to material loss during the cutting process. The correction coefficient, C_i , was based on the weight of lost material per sample:

$$C_i = \frac{W_0}{W_i}, \quad (2.4)$$

where W_0 is the weight of a precisely 10 mm long sample of BRAN rod and W_i is the measured weight of the i^{th} sample. The activity of each sample was corrected by applying the correction coefficient

$$A_i^* = C_i \cdot A_i. \quad (2.5)$$

It is assumed that the activity is homogeneous within the sample.

In order to properly map the activity results in the FLUKA simulation, the center of the samples within the BRAN rod prior to cutting was calculated as

$$P_i = L_{rem,i} + L_{loss} + 0.5 \cdot L_i, \quad (2.6)$$

where P_i is the center of the i^{th} sample in the uncut rod, $L_{rem,i}$ is the length of the remaining uncut rod after the i^{th} cut and L_i is the length of the i^{th} sample, calculated using Eq. 2.1. The amount of rod lost due to cutting, L_{loss} , is assumed to be equal to the width of the saw blade, 0.38 mm¹. P_i was calculated immediately after each cut, allowing for an accurate measure of L_i^{rem} .

¹Please note that, for the first and the last cuts of the rod, L_{loss} is assumed to be 0.19 mm since those segments are obtained with only one cut.

2.2.5.4 Cooling correction

The isotope activity for each sample was estimated making use of UIUC and ANL measurements separately. To allow for comparison of estimates done for a given segment, as well as comparison between the measurements and the FLUKA simulations, the activity for all samples was normalized to the same reference date (12/14/2019).

The Beer–Lambert law [29] is used to extrapolate the activity to the reference date:

$$A_t = A_0 e^{-\lambda t}, \quad (2.7)$$

where A_t is the activity on the reference date, A_0 is the activity on the measurement date, t is the time between the measurement and reference date, and λ is the decay constant of the isotope being measured. For the ^{22}Na isotope considered in this study, the decay constant is 0.2664 yr^{-1} .

2.2.6 Results and discussions

The comparisons between the ^{22}Na activity measurements done at UIUC (HPGe) and ANL (well-type detector) for Rods 1, 3b and 6 are shown in Fig. 2.3, 2.4, and 2.5, respectively. At this stage, both the results are not corrected for material losses. The blue and red curves represent the activity of each segment measured with the HPGe and well-type detector, respectively. Due to the crossing angle in 2017 and 2018, the peak of the activity centers around 5 cm from the bottom of the rod. The lower portion of the figures shows the ratio between the two measurements, fitted with a constant function to demonstrate the consistency between the two curves.

Fig. 2.6, 2.7, and 2.8 show the activity per volume comparison between the measurement and simulation for Rods 1, 3b, and 6 respectively. The blue curve represents the data collected using the well-type detector, while the red curve corresponds to the simulation result obtained from FLUKA. The experimental results are corrected for material losses (Sec. 2.2.5.3). Both experimental and simulation results are normalized to the same reference date, as described in Sec. 2.2.5.4. The relative statistical uncertainty for simulation and

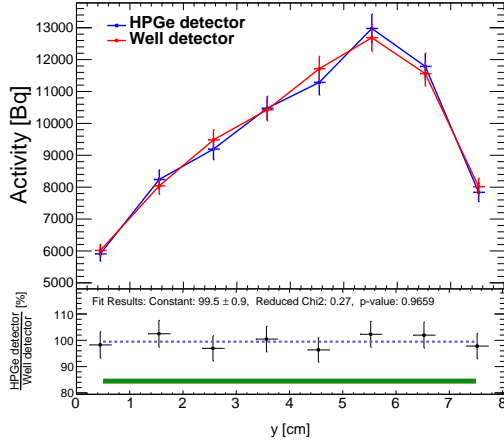


Figure 2.3: Comparison of Rod 1 activity measurements performed at UIUC, using a HPGe detector (Sec. 2.2.3), and ANL, using a well-type detector (Sec. 2.2.4). The dotted line is the fit of the ratio between the two measurements. The green line represents the error on calibration source activity. This uncertainty is not independent between the two measurements. Results have been normalized to a reference date of 12/14/2019.

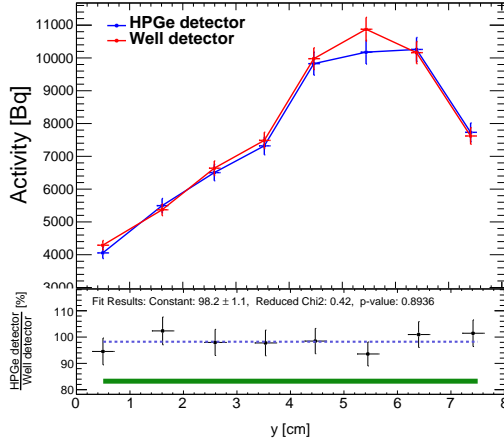


Figure 2.4: Comparison of Rod 3b activity measurements performed at UIUC, using a HPGe detector (Sec. 2.2.3), and ANL, using a well-type detector (Sec. 2.2.4). The dotted line is the fit of the ratio between the two measurements. The green line represents the error on calibration source activity. This uncertainty is not independent between the two measurements. Results have been normalized to a reference date of 12/14/2019.

experimental results is 5% and 3.3%, respectively. The simulation reproduces the peak of activity observed in the experimental measurements around 5 cm. For Rod 1 and 6, there is a 60 to 80% difference between the measurements and the simulation in the activity per volume. For Rod 3b, the discrepancy increases up to 90%.

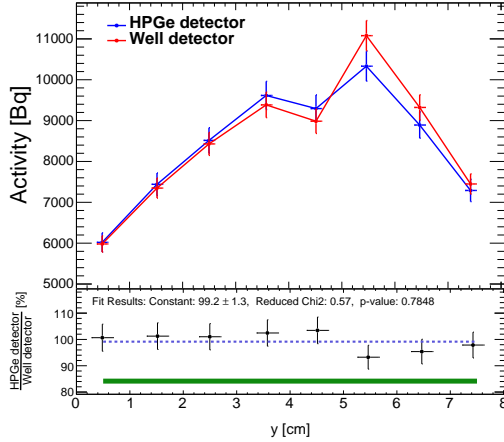


Figure 2.5: Comparison of activity Rod 6 measurements performed at UIUC, using a HPGe detector (Sec. 2.2.3), and ANL, using a well-type detector (Sec. 2.2.4). The dotted line is the fit of the ratio between the two measurements. The green line represents the error on calibration source activity. This uncertainty is not independent between the two measurements. Results have been normalized to a reference date of 12/14/2019.

2.3 Transmission measurements for the BRAN samples

2.3.1 Experimental setup

An optical transmission measurement along the BRAN rods was carried out to investigate the correlation between the dosage and the transmittance degradation. The experimental setup is shown in Fig. 2.9. A light source, a sample holder, and a spectrometer were connected by optical multi-mode fibers [30]. There are two LA4647 lens [31] installed in the holder. One lens collimates the light of the fiber from the light source while the other lens focuses the light from the sample to the fiber of the spectrometer. The light source is Ocean Insight DH-2000-BAL [32], a combination of deuterium and tungsten halogen lamps. The spectrometer is a charge-coupled device spectrometer, Thorlab CCS 200 [33]. The targeted wavelength is 200 nm - 1024 nm in the measurement. The light is incident on the side of the sample since the cutting surface was not polished in the current stage.

The integration time is 120 ms for each measurement. The spectral intensity result is the average of 100 measurements. An un-irradiated sample was used as a reference sample to calculate the transmittance of the irradiated samples. A baseline of the spectrometer was

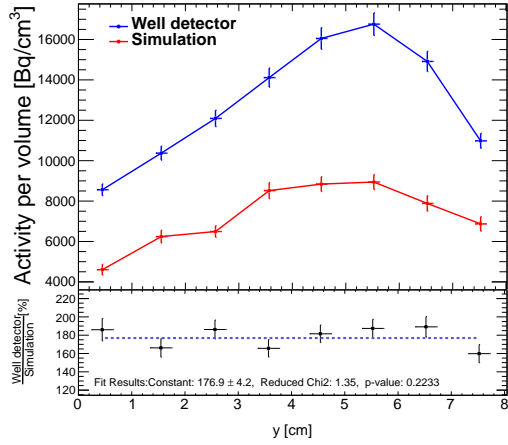


Figure 2.6: Comparison of activity measurements at ANL, using a well-type detector, and FLUKA simulations for Rod 1. Results have been normalized to a reference date of 12/14/2019. The dotted line is the fit of ratio between data and simulations.

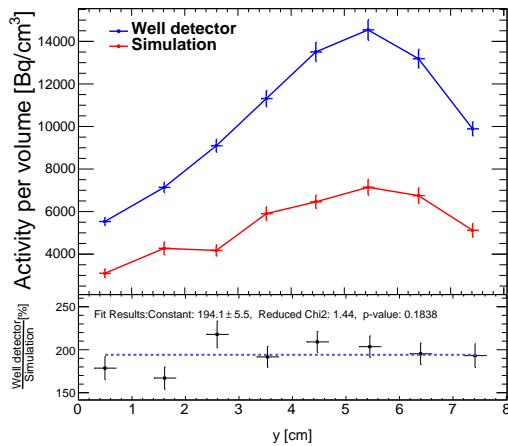


Figure 2.7: Comparison of activity measurements at ANL, using a well-type detector, and FLUKA simulations Rod 3b. Results have been normalized to a reference date of 12/14/2019. The dotted line is the fit of ratio between data and simulations.

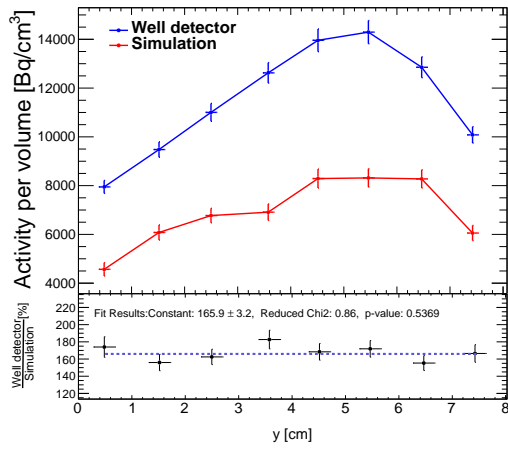


Figure 2.8: Comparison of activity measurements at ANL, using a well-type detector, and FLUKA simulations Rod 6. Results have been normalized to a reference date of 12/14/2019. The dotted line is the fit of ratio between data and simulations.

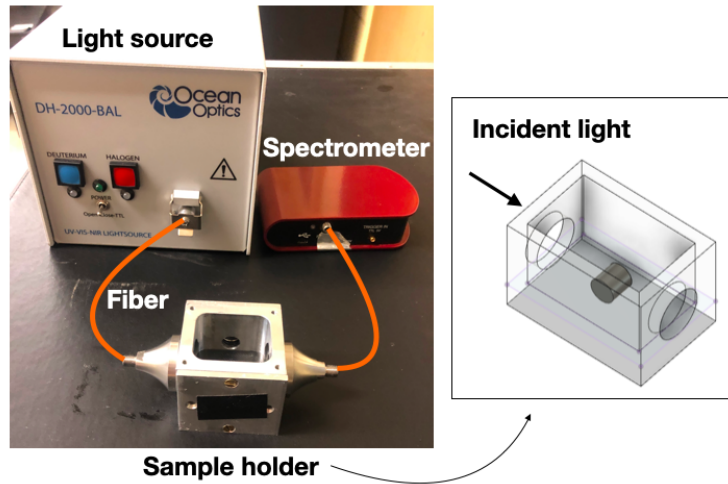


Figure 2.9: The experimental setup for the transmission measurement. The right insert shows interior of the holder. The solid cylindrical volume indicates the position of the sample inside the holder. The light is incident on the curved side of the sample.

measured using a shutter in the light source.

2.3.2 Results and discussions

Fig 2.10 shows the spectrum of reference, baseline, and a Rod 3b sample. The center of the sample corresponds to 4.5 cm from the highly irradiated end of the uncut rod. The location of the sample was received the highest dosage within the rod in 2017 and 2018.

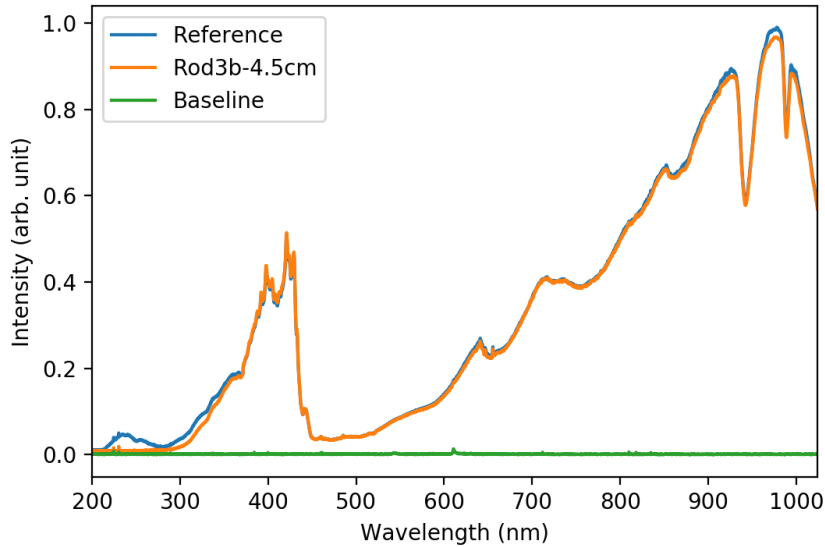


Figure 2.10: The spectral intensity of the reference sample, the baseline, and a Rod 3b sample. The center of the Rod 3b sample corresponds to 4.5 cm from the highly irradiated end of the uncut rod.

The transmittance T is determined as:

$$T = \frac{I_{sample} - I_{baseline}}{I_{ref} - I_{baseline}}, \quad (2.8)$$

where I_{sample} , I_{ref} and $I_{baseline}$ represent the intensity of the rod sample, the reference sample, and the baseline, respectively.

Fig. 2.11 shows the spectral transmittance of the Rod 3b sample. One can observe the transmittance above 400 nm is around 1.0 and drops to 0.2 in the wavelength range from 400 nm to 240 nm. The lowest transmittance in the whole spectrum is located at 240 nm, so

the transmittance at 240 nm can represent a lower bound of the transmittance degradation for the whole rod. Fig. 2.12 shows that the transmittance profile at 240 nm for Rod 1, 3b, 5, 6, respectively. Based on the transmittance curves for each rod, the transmittance decays as the integrated dosage increases. However, in the first 10 cm, where the highest dosage occurs during irradiation, the degradation of transmittance stops around 0.2. The observation is consistent with results in [34], which the signal gain became stable, and no significant loss was observed even with more irradiation.

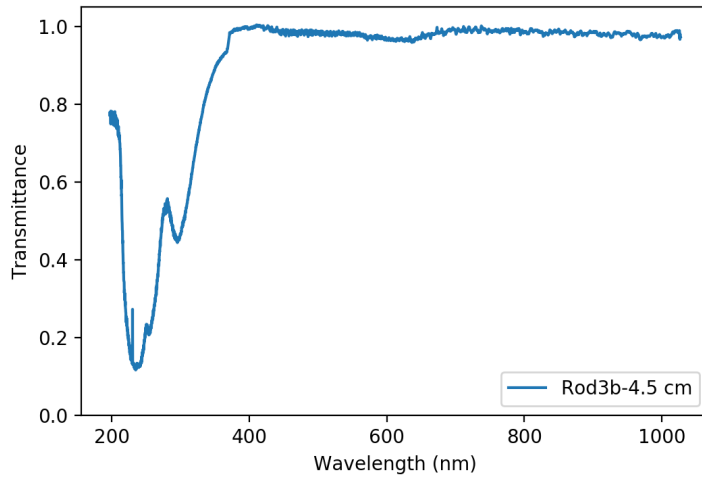


Figure 2.11: The spectral transmittance of the 2.5 cm of Rod 3b. There are 2 color centers (valleys) at 240 and 320 nm.

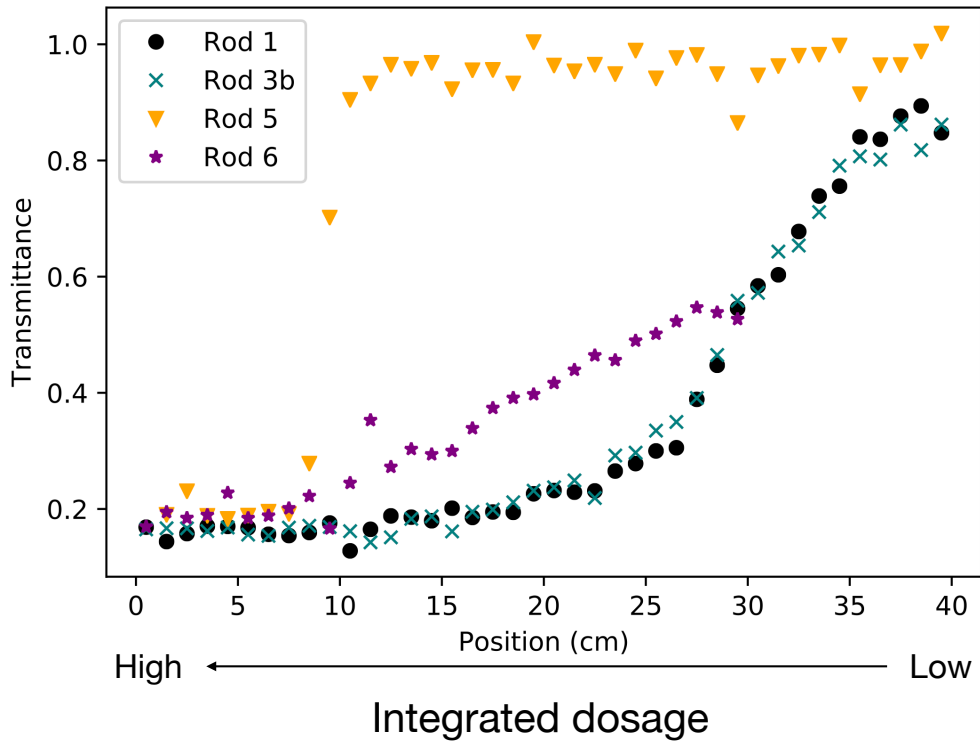


Figure 2.12: The transmittance at 240 nm color center for Rod 1, 3b, 5 and 6. The position starts from the highly irradiated end. The transmittance decays as the integrated dosage increases.

CHAPTER 3

REACTION PLANE RECONSTRUCTION FOR RPD

This chapter presents a reconstruction method for the reaction plane angle for the RPD in the ZDC module. A machine learning (ML) algorithm is used to reconstruct the reaction plane angle using the RPD signals generated from dedicated heavy-ion collision MC simulations in Joint ZDC Calorimeter Project Analysis (JZCaPA) [35, 36].

3.1 Simulation setup

3.1.1 ZDC module

Fig. 3.1 shows the setup of a ZDC module placed at ± 127 m from the interaction point. The upstream electromagnetic (EM) section in the ZDC consists of 25 layers of 4 mm thick tungsten plates, and 26 layers of 0.7 mm diameter fused silica fibers. The downstream hadronic (HAD) section in the ZDC is made of 11 layers of 10 mm thick tungsten plates, and 12 layers of 0.7 mm diameter fused silica fiber. The RPD is installed after the EM section to capture the transverse profile created in the EM section by spectator neutrons. To reduced the simulation time, only the first HAD section, the EM section, and the RPD were simulated.

3.1.2 RPD design

The RPD is comprised of 256 overlapping fibers that can be treated as a virtual 4×4 array of squared tiles, each with a 9.60 mm side. Each tile is comprised of 16 synthetic fused silica fibers, situated perpendicular to the LHC beam and arranged to lie at the same height in y .

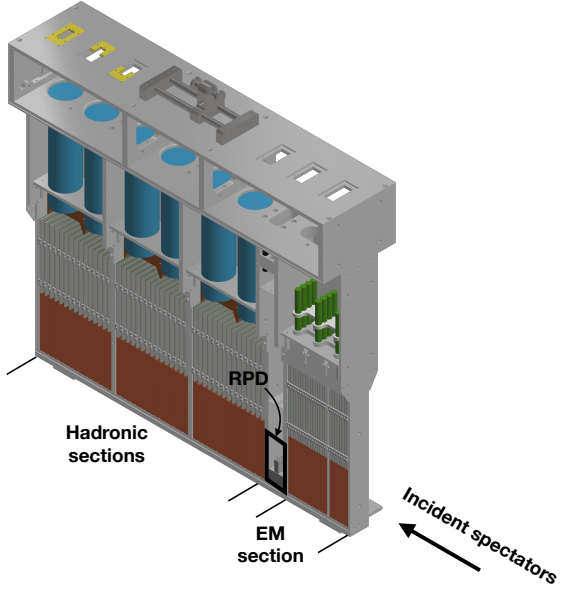


Figure 3.1: The ZDC module consists the electromagnetic (EM), RPD, and the hadronic (HAD) sections.

The fibers in the same tile are routed upwards (in y) for 413 mm, where they are read out by a PMT. For a visual representation of the geometry of the fibers, see Fig. 3.2.

3.1.3 Simulation of directed flow

Directed flow tends to lead to a correlated deflection of the spectators. A simple generation mechanism was implemented to introduce directed flow effects in the distribution of the generated spectators into the JZCaPA Geant4 Monte-Carlo. Event-by-event fluctuations in the number of neutrons are obtained by sampling a Poisson distribution with $\lambda = 30$ to determine the number of spectators. This value was chosen to emulate the spectator multiplicity in mid-central heavy-ion collisions. The initial momenta (P_x , P_y , P_z) of each neutron are assigned independently to simulate the Fermi motion of the neutron in a nucleus. Then, the neutrons are boosted along the longitudinal (z) direction into a collider frame. After generating the momenta of the neutrons in the collider frame, the neutron directed flow is introduced as an additional transverse ($x-y$) momentum kick (applied to each neutron momentum vector) along the direction of the reaction plane, p_T^{spec} . The magnitude of the kick was uniformly distributed between 5 MeV and 50 MeV for the current studies. This

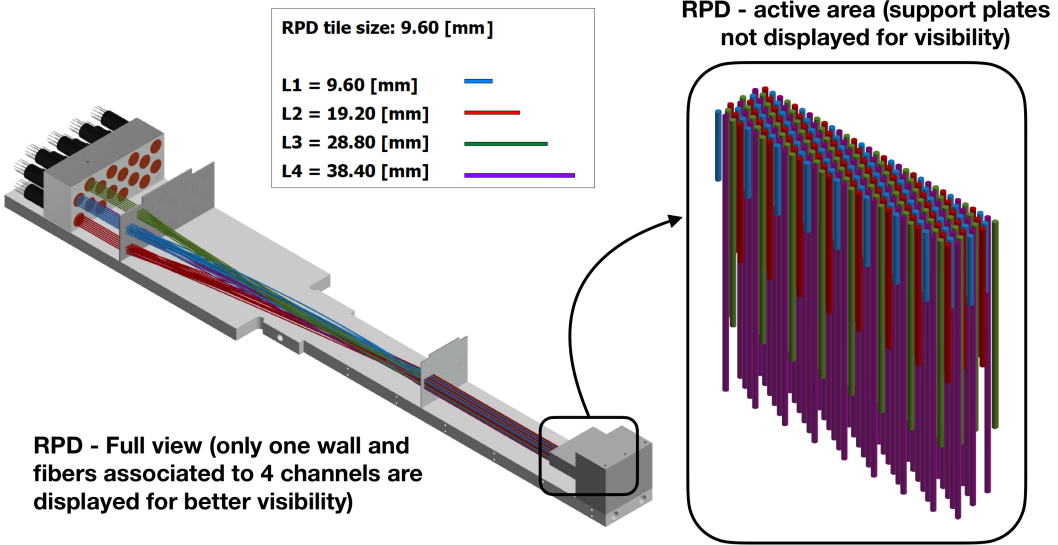


Figure 3.2: The fiber channel pattern of the RPD routed to the PMT above. The right insert shows the arrangement of the fibers in the detector. Different fiber colors identify fibers of different length.

range was constructed around a reference measurement performed by ALICE at 2.76 TeV [37]. After defining the kinematics in this way, the neutrons are injected in the Geant4 simulation and propagated towards both the ZDCs installed in the opposite direction with respect to the IP, hereafter referred to as arm A and arm C.

3.1.4 Digitization and waveform analysis

In the simulation, the Cherenkov light is generated when charged particles pass through the RPD fibers. The lights propagate in the fiber and, arriving at PMT are converted to a digital waveform to mimic the data format in the real experiments at LHC. Each photon reaching the PMTs is converted to a pulse with an integrated area of 1 pC for a 5GHz sampling rate. The sampling rate is based on an analog-to-digital evaluation board [38]. To account for the PMT response for different photon energies, the pulse's maximum amplitude is scaled by the photon energy and the corresponding PMT's quantum efficiency at the photon wavelength. Each scaled pulse is also delayed by the time difference with respect to the first arriving photon in each event. The output signal is generated from the superposition of each waveform of the arriving photons. Dark currents and the Gaussian noise are added to

the output waveform to account for the electronic noise. ¹The digitization process is applied to all the channels of the RPD. Note that the gain for all the PMTs is assumed to be the same in the current setup. More detailed information can be found in [40]. The charge of the integrated digitized waveforms of readout channels is extracted by JZCaPA [35].

3.2 Reaction plane reconstruction

The reaction plane can be estimated from a flow vector Q , [10] and the reaction plane angle ψ is defined by the equations:

$$\begin{aligned} Q_x &= Q \cos \psi = \sum_i w_i \cos \phi_i, \\ Q_y &= Q \sin \psi = \sum_i w_i \sin \phi_i, \end{aligned} \tag{3.1}$$

where the sum is over the neutrons detected in a ZDC arm in a given event. ϕ_i is the azimuthal angles of the i^{th} spectator, and w_i is the corresponding weight. It is customary to optimize w_i to produce the best possible reaction plane resolution. In practice, the w_i is calculated from the detector signals [41, 37]. Since the structure of the RPD signals can be interpreted as pixels of an image, it is possible to apply ML techniques such as pattern recognition and computer vision [42] to optimize the weights for the flow vectors.

3.2.1 Machine learning for directed flow vector reconstruction

Machine learning algorithms have shown significant performance improvements compared to other traditional methods [43]. The deep learning algorithm is particularly promising in the presence of large data samples, high dimensionality data, and complex dependencies between inputs and outputs [44], as is the case for the RPD data.

A convolutional neural network (CNN) algorithm [45] was chosen to perform the reaction plane reconstruction using the RPD signals. The whole model is composed of two input branches, "RPD signals" and "Total neutron", and one predictive branch to estimate the

¹The dark current and noise level is chosen based on Hamamatsu R2496 PMT [39]

Q -vector in a unit length. The model structure is shown in Fig. 3.3. The "RPD signals" branch contains 7 learned layers - 2 convolutional and 5 fully-connected. This branch takes the signals of the 16 channels from RPD and processes them as an image to extract the relation of neighboring channels. The "Total neutron" branch is provided with the number of incident neutrons, which can be estimated from the deposited energy in the ZDCs during the experiments. These two branches are combined and fed to the following predictive branch. The last linear layer in the predictive branch estimates the Q -vector in terms of a 2-dimensional unit vector. (see Eq. 3.1).

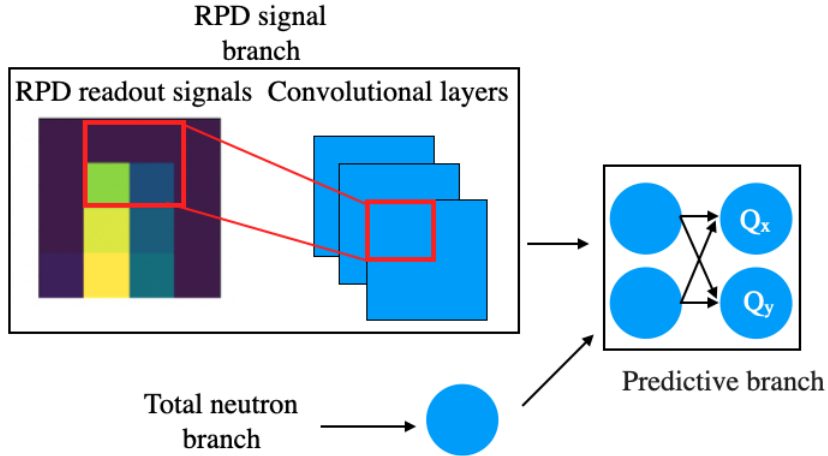


Figure 3.3: Visualization of the deep learning model for reaction plane reconstruction.

Here we define the computing methods for the reaction plane angle in this study:

1. Truth - the true reaction plane angle predefined in the MC simulations. This is used to determine the direction of the transverse momentum kick, p_T^{spec} , when generating the spectators' momenta.
2. Gen - the reaction plane angle computed from the average positions of injected spectators in the MC simulations. This method includes the event-by-event fluctuation.
3. Rec - the reaction plane angle reconstructed by the machine learning model using RPD signals.

Fig. 3.4 shows the visualization of Q -vector for the computing methods.

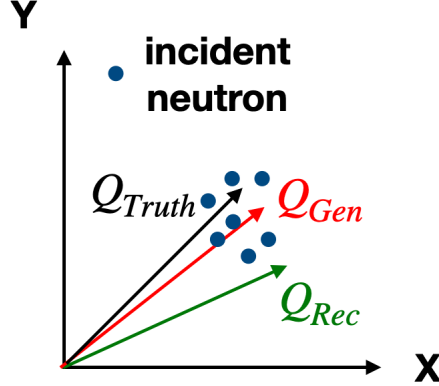


Figure 3.4: Visualization of the Q-vector for the computing methods. The blue dots indicate the injected neutron position in the simulation.

For the model training, the target of the model is to estimate the event-by-event Q^{Gen} . The loss function between target and estimation is the mean absolute error function. 0.8 and 0.2 million events from each ZDC-A and ZDC-C were used for the training set and the testing set.

3.2.2 Results

The reaction plane angle ψ_0^i can be estimated from the corresponding Q-vector as [46]:

$$\psi_0^i = \arctan \frac{Q_y^i}{Q_x^i}, \quad (3.2)$$

where ψ_0^i and Q^i represent the the reaction plane angle and the Q-vector from the i^{th} method in described Sec. 3.2.1.

The performance of the model can be evaluated by the standard deviation, $\sigma_{residual}$, of a Gaussian fit of the residuals between two generating methods, i.e., $\psi_0^{Gen} - \psi_0^{Rec}$, performed in a range defined as \pm standard deviation of the distribution around the mean. The residuals between the ψ_0^{Gen} and ψ_0^{Rec} are shown in the left panel of Fig. 3.5 and the residuals between the ψ_0^{Truth} and ψ_0^{Rec} are presented in the right panel of the same figure.

The reaction plane resolution can be calculated by making use of independent sub-reaction planes measured for each event [47]. In the specific case of the ZDC, the two reaction

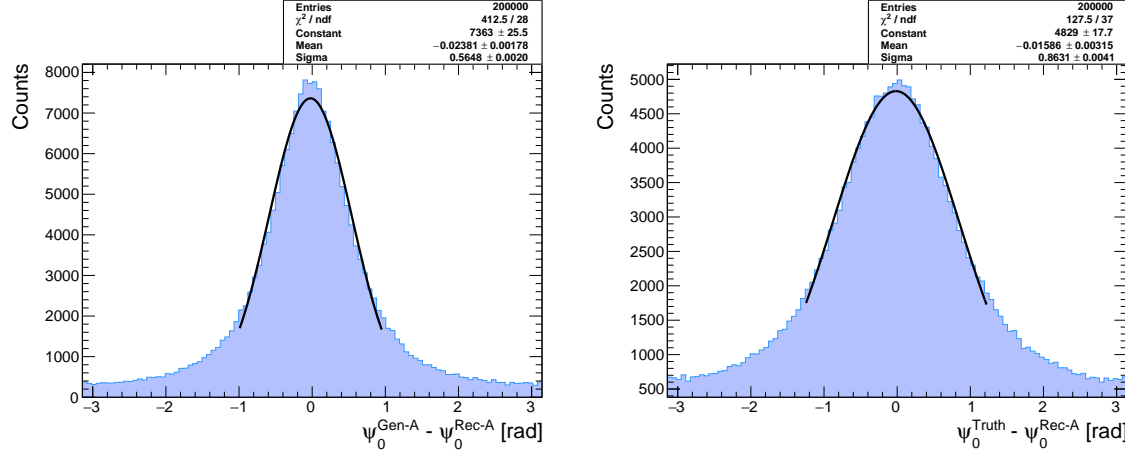


Figure 3.5: Residuals distribution between the the particle level RP angle and the RP angle measured by arm A of the ZDC (left) and the true RP angle and measured RP(right).

plane angles are measured by the two arms of the ZDC (A and C). Under the reasonable assumption that the two sub-reaction plane angles have the same resolution, the correlation between these two reaction plane angles for the directed flow can be expressed as [41]:

$$\langle \cos[(\psi_0^{\text{Sub}} - \psi_0^{\text{Truth}})] \rangle = \sqrt{\langle \cos[(\psi_0^{\text{A}} - \psi_0^{\text{C}})] \rangle}, \quad \text{Sub} = \{\text{A, C}\}, \quad (3.3)$$

where ψ_0^{A} and ψ_0^{C} are the reaction plane angles measured by ZDC-A and ZDC-C, respectively. Note Eq. 3.3 equaling 1.0 would denote a perfect resolution. The reaction plane angle resolution can be obtained by making use of an RPD in both arms using Eq. 3.3. Fig 3.6 shows the resolution results binned into different neutron multiplicity and the transverse momentum selections. The overall resolution, integrating over the number of neutrons, are given in the figure for $p_T^{\text{spec}} = 5\text{-}15, 15\text{-}25, 25\text{-}35, 35\text{-}50$ MeV, respectively.

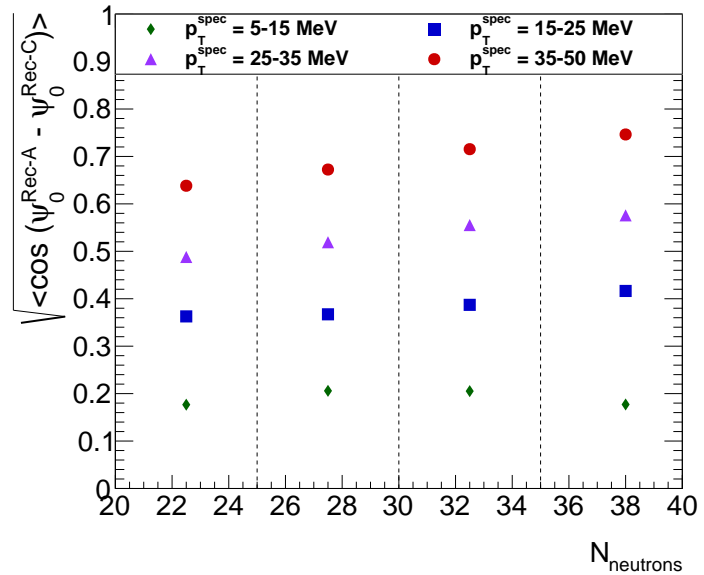


Figure 3.6: Reaction plane resolution estimated using the two sub-reaction planes [10] measured by the two arms of the ZDC. The results are presented for four different simulations where the transverse momentum kick along the direction of the reaction plane, p_T^{spec} , was varied. The vertical dashed lines correspond to the limits of the four bins in neutron multiplicity where the resolution was evaluated. Error bars are contained within the markers.

CHAPTER 4

CONCLUSIONS AND FUTURE WORK

The HL-LHC upgrade opens new frontiers for more precise, as well as novel, physics measurements. On the other hand, it creates many challenges regarding the detector technology to be deployed to cope with the higher luminosity. One of these challenges is the radiation-hardness of the ZDC used in the ATLAS. The current fused quartz ZDC rods are not sustainable for the HL-LHC upgrade because of the significant transmittance degradation induced by radiation damage. Ultra-pure fused silica was identified as an alternative radiation-hard Cherenkov radiator for the ZDCs in the HL-LHC. The optical transmission and activity measurements of the fused silica rods installed in the BRAN prototype are presented in this work, together with a Machine Learning (ML) reaction plane reconstruction method for the ZDC Reaction Plane Detector (RPD). The final transmission results define the expectations for the ZDC performance stability during the running time, while the activity results represent a benchmark for the accuracy of nuclear breakup model on a wide energy range (up to the TeV scale) in FLUKA. The ML based reconstruction algorithm developed for the UIUC design of the RPD will allow for a meaningful measurement of the reaction plane in ATLAS, opening the possibility for a wide range of new flow-related physics analysis.

The study of the BRAN rod activation is being drafted for publication. I am currently discussing with EN-STI-BMI team the possibility of fine-tuning the nuclear break-up description in FLUKA.

To accurately measure the transmittance per unit length of the BRAN rods, the latter were cut in segments of about 1 cm length each, to measure the transmission longitudinally through each sample. An index refractive matching liquid will be used to remove the roughness of the cutting surface to approximate a polished surface. Another independent measurement was setup and is currently being conducted at the UIUC Material Research

Laboratory, to independently verify the results. Once obtained, those will be compared to the dosage of the FLUKA simulations to study the correlation between transmission degradation and dosage induced by different particle species.

The capability of the ML based reconstruction algorithm will be tested using the experimental data of the test beam campaign planned at the CERN SPS in Fall 2021. The proposed RPD will be installed in the H4 beam-line at SPS North Area to test the detector response using a 350 GeV proton beam, as well as a 250 GeV electron beam. Different sets of beam scans will be recorded, varying the impinging point on the ZDC and therefore the transverse shower profile sampled by the RPD. The detector signals and the reconstructed beam positions in the experiment can be used as a test set for the ML reconstruction method. A dedicated MC simulation for the experimental setup in the campaign will be carried out to generate the RPD signal and the beam position as a training set for the ML model. The latter will be trained on the simulation output to estimate the incident beam position. After the model is trained, the experimental RPD signal will be fed to the model to estimate the beam position on a event-by-event basis. The residuals between estimated and recorded beam positions will be used to evaluate the performance of ML algorithm ¹.

¹The work was used as input to a proposal presented to the ATLAS and CMS collaborations. That both collaborations have approved the plans for the ZDC and RPD for Run 4. We are currently applying for a \$1.5M grant from DOE to carry out the construction. The proposal can be accessed here: <https://uofi.box.com/s/kdsmthhm5tguwtrprl2ihg508x03yn1m>

CHAPTER 5

REFERENCES

- [1] L. Evans and P. Bryant, “LHC machine,” *Journal of instrumentation*, vol. 3, no. 08, p. S08001, 2008.
- [2] H. Burkhardt and I. Efthymiopoulos, “Interface with experiments,” *arXiv preprint arXiv:1705.09492*, 2017.
- [3] G. Aad, J. Butterworth, J. Thion, U. Bratzler, P. Ratoff, R. Nickerson, J. Seixas, I. Grabowska-Bold, F. Meisel, S. Lokwitz *et al.*, “The ATLAS experiment at the CERN large hadron collider,” *Jinst*, vol. 3, p. S08003, 2008.
- [4] S. Chatrchyan, G. Hmayakyan, V. Khachatryan, C. Collaboration *et al.*, “The CMS experiment at the CERN LHC,” *Journal of instrumentation*, vol. 3, no. 8, p. S08004, 2008.
- [5] K. Aamodt, A. A. Quintana, R. Achenbach, S. Acounis, D. Adamová, C. Adler, M. Aggarwal, F. Agnese, G. A. Rinella, Z. Ahammed *et al.*, “The ALICE experiment at the CERN LHC,” *Journal of Instrumentation*, vol. 3, no. 08, p. S08002, 2008.
- [6] L. Collaboration, A. A. Alves, L. A. Filho, A. Barbosa, I. Bediaga, G. Cernicchiaro, G. Guerrer, H. Lima, A. Machado, J. Magnin *et al.*, “The LHCb detector at the LHC,” *Journal of instrumentation*, vol. 3, no. 08, pp. S08 005–S08 005, 2008.
- [7] P. Jenni, M. Nessi, and M. Nordberg, “Zero degree calorimeters for ATLAS,” CM-P00072881, Tech. Rep., 2007.
- [8] M. A. Leite, “Performance of the ATLAS zero degree calorimeter,” in *2013 IEEE Nuclear Science Symposium and Medical Imaging Conference (2013 NSS/MIC)*. IEEE, 2013, pp. 1–5.
- [9] W. Reisdorf and H. Ritter, “Collective flow in heavy-ion collisions,” *Annual Review of Nuclear and Particle Science*, vol. 47, no. 1, pp. 663–709, 1997.
- [10] A. M. Poskanzer and S. A. Voloshin, “Methods for analyzing anisotropic flow in relativistic nuclear collisions,” *Physical Review C*, vol. 58, no. 3, p. 1671, 1998.
- [11] W. Herr and B. Muratori, “Concept of luminosity,” 2006.
- [12] “The HL-LHC project: High luminosity large hadron collider.” [Online]. Available: <https://hilumilhc.web.cern.ch/>

- [13] G. Apollinari, O. Brüning, T. Nakamoto, and L. Rossi, “High luminosity large hadron collider HL-LHC,” *arXiv preprint arXiv:1705.08830*, 2017.
- [14] M. W. Phipps, “A new ATLAS ZDC for the high radiation environment at the LHC,” ATL-COM-FWD-2018-006, Tech. Rep., 2018.
- [15] “Luminosity results for Run-1 (2010-2012).” [Online]. Available: <https://twiki.cern.ch/twiki/bin/view/AtlasPublic/LuminosityPublicResults>
- [16] S. Jakobsen, “BRAN prototype for IP1,” BE-BI-PM, 2016. [Online]. Available: https://indico.cern.ch/event/503430/contributions/1180735/attachments/1234188/1811265/BRAN_prototype_for_IP1_small.pdf
- [17] “Data and properties optics fused silica,” Heraeus. [Online]. Available: https://www.heraeus.com/media/media/hca/doc_hca/products_and_solutions_8/optics/Data_and_Properties_Optics_fused_silica_EN.pdf
- [18] M. Palm, “Update on luminosity monitoring for HL-LHC,” 2017. [Online]. Available: https://indico.cern.ch/event/647714/contributions/2651509/attachments/1557659/2450420/Palm_HL-LHC_2017_BRAN.pdf
- [19] G. Battistoni, F. Cerutti, A. Fasso, A. Ferrari, S. Muraro, J. Ranft, S. Roesler, and P. Sala, “The FLUKA code: Description and benchmarking,” in *AIP Conference proceedings*, vol. 896, no. 1. American Institute of Physics, 2007, pp. 31–49.
- [20] R. G. Alía, M. Brugger, F. Cerutti, S. Danzeca, A. Ferrari, S. Gilardoni, Y. Kadi, M. Kastriotou, A. Lechner, C. Martinella *et al.*, “LHC and HL-LHC: Present and future radiation environment in the high-luminosity collision points and RHA implications,” *IEEE Transactions on Nuclear Science*, vol. 65, no. 1, pp. 448–456, 2017.
- [21] T. Böhlen, F. Cerutti, M. Chin, A. Fassò, A. Ferrari, P. Ortega, A. Mairani, P. Sala, G. Smirnov, and V. Vlachoudis, “The FLUKA code: Developments and challenges for high energy and medical applications,” *Nuclear Data Sheets*, vol. 120, pp. 211 – 214, 2014. [Online]. Available: <http://www.sciencedirect.com/science/article/pii/S0090375214005018>
- [22] G. Battistoni, F. Broggi, and V. Boccone, “FLUKA capabilities and CERN applications for the study of radiation damage to electronics at high-energy hadron accelerators,” *Progress in Nuclear Science and Technology*, vol. 2, pp. 948–954, 2011.
- [23] R. Rata, R. Barlow, and S. Lee, “FLUKA simulations for radiation protection at 3 different facilities,” in *7th Int. Particle Accelerator Conf.(IPAC’16), Busan, Korea, May 8-13, 2016*. JACOW, Geneva, Switzerland, 2016, pp. 1940–1942.
- [24] J. Wenninger and M. Hostettler, “LHC report: colliding at an angle.” [Online]. Available: <https://home.cern/news/news/accelerators/lhc-report-colliding-angle>
- [25] “Luminosity results for Run-2 (2016-2018).” [Online]. Available: <https://twiki.cern.ch/twiki/bin/view/AtlasPublic/LuminosityPublicResultsRun2>

- [26] M. Brugger, A. Ferrari, S. Roesler, and L. Ulrici, “Validation of the FLUKA monte carlo code for predicting induced radioactivity at high-energy accelerators,” *Nuclear Instruments and Methods in Physics Research Section A: Accelerators, Spectrometers, Detectors and Associated Equipment*, vol. 562, no. 2, pp. 814–818, 2006.
- [27] E. Iliopoulou, P. Bamidis, M. Brugger, R. Froeschl, A. Infantino, T. Kajimoto, N. Nakao, S. Roesler, T. Sanami, and A. Siountas, “Measurements and FLUKA simulations of bismuth and aluminium activation at the CERN shielding benchmark facility (CSBF),” *Nuclear Instruments and Methods in Physics Research Section A: Accelerators, Spectrometers, Detectors and Associated Equipment*, vol. 885, pp. 79–85, 2018.
- [28] “Specifications of 2480 wizard2 - ivd automatic gamma counters,” Perkin Elmer. [Online]. Available: https://www.perkinelmer.com/lab-solutions/resources/docs/SPC_2480-WizardSpecSheetIVD_F.pdf
- [29] J. R. Lamarsh and A. J. Baratta, *Introduction to nuclear engineering*. Prentice hall Upper Saddle River, NJ, 2001, vol. 3.
- [30] “Solarization-resistant multimode fiber optic patch cables.” [Online]. Available: https://www.thorlabs.com/newgroupage9.cfm?objectgroup_id=5591
- [31] “LA4647 - f = 20.1 mm, UV fused silica plano-convex lens, uncoated.” [Online]. Available: <https://www.thorlabs.com/thorproduct.cfm?partnumber=LA4647>
- [32] *DH-2000 Deuterium-Halogen Light Source*, Ocean optics.
- [33] *CCS Series Spectrometer Operation Manual*, Thorlabs.
- [34] M. Palm, “Update on luminosity monitoring for HL-LHC,” BE-BI-PM, 2018. [Online]. Available: https://indico.cern.ch/event/755408/contributions/3153780/attachments/1725682/2787563/2018_HL-LHC_BRAN_MPalm_v0.1.pdf
- [35] Joint ZDC Calorimeter Collaboration, “Joint ZDC calorimeter project analysis,” 2019. [Online]. Available: <https://gitlab.engr.illinois.edu/rlongo/JZCaPA>
- [36] S. Agostinelli, J. Allison, K. a. Amako, J. Apostolakis, H. Araujo, P. Arce, M. Asai, D. Axen, S. Banerjee, G. . Barrand *et al.*, “GEANT4—a simulation toolkit,” *Nuclear instruments and methods in physics research section A: Accelerators, Spectrometers, Detectors and Associated Equipment*, vol. 506, no. 3, pp. 250–303, 2003.
- [37] ALICE Collaboration *et al.*, “Directed flow of charged particles at mid-rapidity relative to the spectator plane in Pb-Pb collisions at $\sqrt{s_{NN}}=2.76$ TeV,” *arXiv preprint arXiv:1306.4145*, 2013.
- [38] S. Ritt, “DRS4 evaluation board user’s manual,” 2016. [Online]. Available: https://www.psi.ch/sites/default/files/import/drs/DocumentationEN/manual_rev50.pdf
- [39] “Photomultiplier tube r2496 specification.” [Online]. Available: <https://www.hamamatsu.com/jp/en/product/type/R2496/index.html>

- [40] C. Lantz, “Zdcdigitizer.” [Online]. Available: <https://gitlab.engr.illinois.edu/clantz2/zdcdigitizer/-/blob/master/outputDigitization.cc>
- [41] I. Selyuzhenkov, A. Collaboration *et al.*, “Charged particle directed flow in pb–pb collisions at $\sqrt{s_{NN}}=2.76$ TeV measured with alice at the lhc,” *Journal of Physics G: Nuclear and Particle Physics*, vol. 38, no. 12, p. 124167, 2011.
- [42] C. M. Bishop, *Pattern recognition and machine learning*. springer, 2006.
- [43] Y. Bengio, *Learning deep architectures for AI*. Now Publishers Inc, 2009.
- [44] D. Bourilkov, “Machine and deep learning applications in particle physics,” *International Journal of Modern Physics A*, vol. 34, no. 35, p. 1930019, 2019.
- [45] Y. LeCun, Y. Bengio, and G. Hinton, “Deep learning,” *nature*, vol. 521, no. 7553, pp. 436–444, 2015.
- [46] S. A. Voloshin, A. M. Poskanzer, and R. Snellings, “Collective phenomena in non-central nuclear collisions,” *arXiv preprint arXiv:0809.2949*, 2008.
- [47] P. Danielewicz and G. Odyniec, “Transverse momentum analysis of collective motion in relativistic nuclear collisions,” *Physics Letters B*, vol. 157, no. 2-3, pp. 146–150, 1985.